ACS APPLIED MATERIALS & INTERFACES

www.acsami.org

Research Article

Linking Pressure to Electrochemical Evolution in Solid-State Conversion Cathode Composites

Elif Pınar Alsaç, Arpan Kumar Sharma, Sun Geun Yoon, Bairav S. Vishnugopi, Congcheng Wang, Talia A. Thomas, Douglas Lars Nelson, Udochukwu D. Eze, Won Joon Jeong, John Harris, Partha P. Mukherjee, and Matthew T. McDowell*

Cite This: ACS Appl. Mater. Interfaces 2026, 18, 1626−1640

Read Online

ACCESS | Metrics & More | Article Recommendations | Supporting Information

ABSTRACT: Conversion-type cathodes, such as sulfur, FeS_2, and FeF_3, offer high theoretical capacities in solid-state lithium batteries but are hindered by substantial volume changes during cycling, leading to interfacial contact loss, crack formation, and microstructural degradation. Here, we investigate the relationships between electrochemical, mechanical, and structural evolution in solid-state electrode composites with these three active materials. Using real-time stack-pressure monitoring, synchrotron X-ray absorption spectroscopy, and electrokinetic modeling, we elucidate how stress evolution is linked to reversible and irreversible redox reactions. Nonlinear stack pressure evolution in cells with sulfur, FeS_2, and FeF_3 electrode composites is found to arise from material-specific volume changes, the balance of volume change between the working and counter electrode, and the formation of distinct reaction intermediates. The three materials exhibit distinct stack pressure evolution, which is closely related to the different reaction processes in the materials, as demonstrated with X-ray absorption spectroscopy measurements. Through mesoscale modeling, we relate the experimental measurements to species evolution at the particle scale and track the dynamic coexistence of intermediate phases. Our findings highlight the importance of designing for volume changes of a given active material in solid-state battery systems.

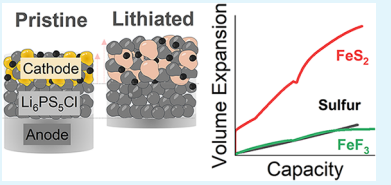

KEYWORDS: *solid-state batteries, conversion cathodes, stack pressure, sulfides, sulfur, pyrite*

INTRODUCTION

While lithium-ion batteries (LIBs) have long been a key energy storage technology, their dependence on flammable liquid electrolytes and their limited energy density pose challenges for meeting growing market demands.[1] Solid-state batteries (SSBs) have emerged as a promising next-generation alternative, prompting the development of new materials and interfacial strategies for effective performance.[2,3] Among cathode active materials (CAMs) for SSBs, intercalation-type oxides, such as $LiNi_xMn_yCo_{1-x-y}O_2$ (NMC), have been extensively studied and are a leading candidate for practical applications due to their stability and reliable performance.[4,5] However, their moderate theoretical capacities (~160−200 mAh g^{-1}), mechanical degradation, and high material costs pose barriers to large-scale deployment, motivating the investigation of alternative cathode active materials.[6−8]

Conversion type cathode materials, including sulfur,[9,10] transition metal sulfides (e.g., FeS_2 and CuS),[11−14] and fluorides (e.g., FeF_2 and FeF_3),[15−18] present a compelling alternative due to their high theoretical capacities enabled by multielectron redox reactions. Sulfur, FeS_2, and FeF_3 exhibit theoretical specific capacities of 1671, 894, and 712 mAh g^{-1}, respectively. These materials show particular promise for SSBs because of the potential for enhanced stability at the electrolyte/electrode interface, as well as the elimination of the polysulfide shuttling effect when using solid electrolytes.[19−22] Recent studies have also emphasized that the practical performance of pyrite-type cathodes is highly dependent on electrode design, including the conductive architecture, the active material particle size, and interfacial optimization, which are important considerations for high capacity cathode composite integration in SSBs.[23,24]

Despite these advantages, conversion cathodes present various challenges due to the insulating nature of material end-members (such as sulfur and Li_2S), the need to maintain physical contact at the electrolyte interface,[25−27] and the substantial volume changes of these materials, which can exceed 100% during lithiation/delithiation.[28−30] Such drastic expansion and contraction can induce significant mechanical stress, leading to interfacial contact loss and/or fracture, which manifest distinctively in SSB systems compared to liquid-electrolyte batteries.[31,32] Prior studies on conversion cathodes have highlighted how mechanical instabilities and microstructural evolution, in tandem with electrochemical reactions,

Received: October 19, 2025
Revised: December 21, 2025
Accepted: December 22, 2025
Published: December 31, 2025

play central roles in capacity fade.[33,34] Additionally, the complex, multistep redox pathways in conversion materials can introduce uneven reaction kinetics and stress distributions, further exacerbating mechanical and electrochemical instabilities.[35−37]

Understanding electro-chemo-mechanical coupling in conversion cathode SSBs is essential for designing stable and long-lasting high-capacity SSBs. Previous investigations have shown that real-time stack pressure monitoring provides useful insights into mechanical evolution during cycling of a variety of types of SSB systems.[35,36,38−43] The uniaxial stress applied to a cell stack (i.e., stack pressure) affects ion transport and interfacial contact.[44−46] Moreover, changes of stack pressure in a constant-volume cell configuration also reflect the volumetric response of the active materials to lithiation/delithiation reactions, making it a key parameter for monitoring electro-chemo-mechanical coupling.[47,48] These insights are particularly important for conversion-type cathodes whose redox reactions involve complex structural transformations and large volume changes. These materials often undergo multistep phase transitions that lead to the formation of intermediate and final products with different (partial) molar volumes and mechanical properties. FeS_2 is particularly notable because it undergoes an irreversible conversion process during the first cycle, producing large and abrupt volume changes that can directly influence stack pressure evolution. As such, the evolution of internal stress is highly sensitive both to the kinetics of these reactions and the evolving electrode microstructure.

Here, we investigate the coupling between electrochemical transformations and stack pressure evolution in sulfur, FeS_2, and FeF_3 electrodes in SSBs. While these materials hold tremendous potential for next-generation SSBs, their electro-chemo-mechanical behavior presents critical challenges that necessitate advanced characterization and modeling to understand and address.[49,50] We used real-time stack-pressure monitoring to track pressure changes and electrochemical signatures, and electron microscopy was used to correlate these factors to microstructure evolution in response to lithiation/delithiation of these materials. X-ray absorption fine structure (XAFS) spectroscopy revealed redox behavior at iron sites in FeS_2 and FeF_3, providing insight into the effects of transition metals on the chemo-mechanics of the conversion process. These results were further contextualized using microkinetic modeling, linking stack pressure evolution to the partial molar volume of intermediate phases and the dynamic coupling between electrochemical processes and mechanical stress. Our findings reveal how the distinct stack pressure evolution behaviors observed using sulfur, FeS_2, and FeF_3 cathodes are closely linked to their underlying redox pathways and microstructural transformations, underscoring the need for material-specific design strategies that mitigate mechanical degradation and enhance interfacial stability in high-capacity SSBs.

EXPERIMENTAL METHODS

Cathode Composite Preparation

Conversion cathode composites were prepared by ball-milling cathode active material (CAM), Li_6PS_5Cl (LPSC, Ampcera, ∼1 μm particle size), and multiwalled carbon nanotubes (MWCNTs, Graphene Supermarket) with a CAM:LPSC:CNT weight ratio of 2:3:1 in a Fritsch Pulverisette 7 planetary ball mill. The CAMs used were sulfur (Thermo Scientific, 325 mesh, 99.5%), FeS_2 (Sigma-Aldrich, 325 mesh, 99.8% trace metals basis), or FeF_3 (Thermo Scientific, anhydrous, 97% min., metal basis). Approximately 1.2 g of the mixture of CAM, LPSC, and MWCNTs was added to a ZrO_2 jar with four 10-mm diameter ZrO_2 balls and 12 g of 1-mm diameter ZrO_2 balls using a 1:20 weight ratio between the composite and ball weight. The mixture was prepared and sealed in the jar within an Ar-filled glovebox before the milling process. Milling was performed at 500 rpm for 24 cycles, with milling for 10 min and resting for 5 min per cycle. After milling, the jar was opened in an Ar-filled glovebox to collect the composite powder.

Counter Electrode Fabrication

Various counter electrodes were used in different cells. Counter electrodes consisting of 20-μm lithium on a 10-μm copper current collector backing (MSE Supplies) were used as-received. A different counter electrode consisted of a mixture of single-crystalline $LiNi_{0.6}Mn_{0.2}Co_{0.2}O_2$ (NMC622) coated with $LiNb_{0.5}Ta_{0.5}O_3$ (LNTO) as the active material (MSE Supplies), LPSC (Ampcera, ∼1 μm particle size), and vapor grown carbon fiber (VGCF, Sigma-Aldrich). LNTO was fabricated and coated on the NMC622 cathode active material before composite preparation to lessen side reactions between the solid electrolyte and the cathode active material. Stoichiometric ratios of lithium acetate ($LiCO_2CH_3$, Sigma-Aldrich, 99.95%), tantalum butoxide ($Ta(OCH_2CH_2CH_2CH_3)_5$, Sigma-Aldrich, 99.99%) and niobium ethoxide ($Nb(OCH_2CH_3)_5$, Sigma-Aldrich, 99.95%) were dissolved in dry ethanol (Sigma-Aldrich, 99.5%) and stirred for 12 h. NMC622 powder was added to this solution and mixed using ultrasonication (Branson 1510 Ultrasonic Cleaner at 40 kHz for 2 h at 25 °C). Then the solvent was evaporated in a vacuum oven for 8 h. 1 mL of solution was added to 2 g of NMC622 powder, followed by heating to 450 °C for 1 min in air. The final composition of the composite was 70 wt % of LNTO-coated NMC622, 27.5 wt % LPSC, and 2.5 wt % VGCF. The mixture was ball-milled (Fritsch Pulverisette 7) at three cycles of 150 rpm for 15 min of milling and 5 min of resting in a ZrO_2 milling jar with eight 1 mm-diameter ZrO_2 milling balls. The jar was sealed and opened after milling in an Ar-filled glovebox.

Solid-State Cell Assembly

90 mg of LPSC powder was loaded in a 10 mm diameter die made from polyether ether ketone (PEEK) and pelletized under uniaxial compression at 150 MPa for 1 min. The sulfur/FeS_2/FeF_3 composite was loaded and repressed at 375 MPa for 5 min and lithium foil was then attached to the opposite side, and the cell was repressed at 60 MPa for 10 min. For the cells prepared with NMC counter electrodes, a two-step pressing protocol was followed. Here, the sulfur/FeS_2/FeF_3 composite and the NMC composite were loaded on top and below the LPSC pellet and pressed at 375 MPa for 10 min. We used 2.0−3.4 mg of active material loading depending on the theoretical specific capacity of the cathode material. To ensure mechanically stable counter electrodes, different areal capacities were selected for Li metal and NMC622. A 20-μm Li foil was used (corresponding to ∼4 mAh cm^{-2}) because this thickness can sustain stack pressure without excessive plastic deformation, whereas thicker Li foils exhibit exacerbated deformation.[51] In contrast, the NMC622 counter electrode featured 6.0 mAh cm^{-2} to operate within a volume-stable regime, thereby minimizing volume changes at this counter electrode.[52] These design choices prevent Li depletion at the solid-electrolyte interface and mitigate interfacial mechanical degradation, enabling representative electrochemical behavior for both cell configurations. A stack pressure of approximately 21 MPa was applied followed by resting for 6 h. All the cells were cycled in an Ar-filled glovebox.

Stress Measurements

Stress measurements were performed in accord with the previously reported procedure.[38] A custom-built cell assembly was used which included a force sensor integrated underneath the cell stack physically separated from the Ti rod using a PEEK plate. The force sensor (2 kN, KMM50, Inelta Sensorsysteme) was paired with a signal conditioner (IMA2-DMS, Inelta Sensorsysteme). The simultaneous

https://doi.org/10.1021/acsami.5c20956
ACS Appl. Mater. Interfaces 2026, 18, 1626−1640

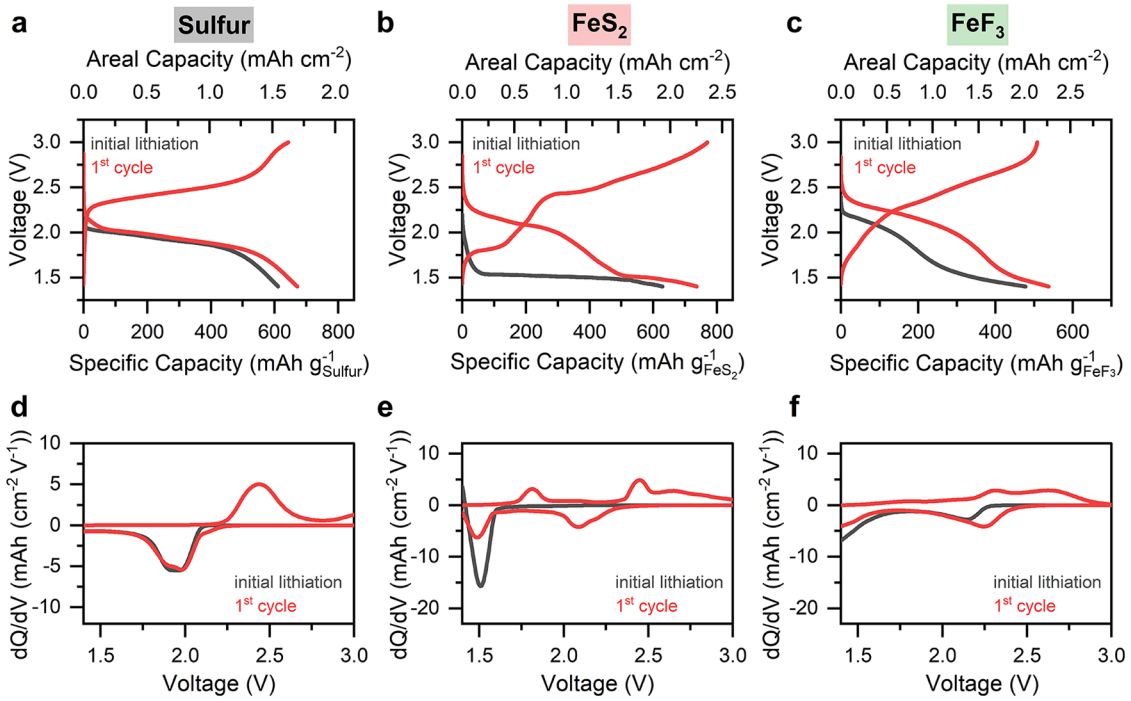

Figure 1. Electrochemical behavior of sulfur, FeS_2, and FeF_3 composite electrodes in solid-state cells with Li_6PS_5Cl solid electrolyte and Li counter electrodes. The experiments were carried out at room temperature using 0.1 mA cm^{-2} current density and 20 MPa stack pressure. (a–c) Charge–discharge profiles of cells with (a) sulfur, (b) FeS_2, and (c) FeF_3 electrode composites. (d–f) Corresponding differential capacity (dQ/dV) curves for each cell in panels a–c.

electrochemical response was recorded using a Landt CT2001 battery tester. The pressure change during cell cycling was recorded with Python. The time derivative of the stress curves (dP/dt) and dQ/dV curves were calculated with OriginLab using Savitsky-Golay smoothing, followed by linear interpolation and differentiation. The cells with Li counter electrodes were cycled between 1.4 and 3.0 V, and the cells with NMC counter electrodes were cycled between −2.5 and 0 V. All of the cells were cycled using 0.1 mA cm^{-2} current density. The areal capacity loading was 4 mAh cm^{-2} for the Li cells and 6 mAh cm^{-2} for the NMC cell. The cells were rested at open circuit for 6 h prior to electrochemical testing.

X-ray Absorption Spectroscopy (XAS)

The *ex situ* XAS experiments on FeS_2 and FeF_3 were performed at the 6-BM Beamline for Materials Measurements (BMM) at the National Synchrotron Light Source II (Brookhaven National Laboratory, NY) using a Si(111) monochromator. Data was collected in fluorescence mode for the Fe K-edge using a four-element Si drift detector. The Athena software package was used for data reduction of the XAS spectra using standard processes.[53] The Artemis software package was used to generate structural models by simulating k^3-weighted extended X-ray absorption fine structure (EXAFS) results between k values of 3 and 12.5 $Å^{-1}$. The location of the Fe K-edges was determined by the half-height method. MorletE software was used for wavelet transform analysis. The cells were run to different states of charge or discharge and then removed from the cells. The disassembled pellets were prepared and sealed in a polymer-covered aluminum pouch cell material to prevent air ingress. The sample surface was covered with Kapton tape as a window to increase the flux of the beam. Samples were prepared in the pristine state, after the first discharge, and after the first charge.

Scanning Electron Microscopy (SEM)

SEM images were collected with a Hitachi SU8230 SEM using an accelerating voltage of 10 kV and a working distance of 8 mm. The cells were sliced with a scalpel to investigate the cross sections of the electrodes. During loading into the SEM, the samples were exposed to the atmosphere for less than 10 s, and evacuation of the loading chamber took around 30 s.

Mechanistic Modeling

The complex, nonlinear electrochemical behavior of conversion cathode cells arises from the coupled effects of interfacial reaction kinetics, ionic transport through the solid electrolyte, and spatially nonuniform species evolution within the composite cathode. These processes span multiple length scales, ranging from particle-scale to the porous electrode microstructure scale, and they are described by the following conservation and reaction equations.[54−56]

The charge conservation equation in the CAM and solid electrolyte (SE) phase is described in eq 1:

$$\nabla i_{SE} + \nabla i_{CAM} = 0 \tag{1}$$

Here, i is the current density in the phase. The distribution of electric potential distribution in the CAM and SE phases is given in eqs 2 and 3:

$$\nabla\cdot(\sigma_s^{eff}\nabla\phi_s) - a_s i_{CAM} = 0 \tag{2}$$

$$\nabla\cdot(\kappa_s^{eff}\nabla\phi_e) + a_s i_{SE} = 0 \tag{3}$$

We assume the following reaction:

$$A \rightarrow B + ne^- + nC^-$$

Here, A, B and C are the species involved in the reaction. The charge transfer reaction rate can be estimated using the Butler–Volmer equation (eq 4, with overpotential defined in eq 5):

$$i = nFk\left\{\varepsilon_A^* \exp\left(\beta\frac{F}{RT}\eta\right) - \varepsilon_B^* \exp\left(-(1-\beta)\frac{F}{RT}\eta\right)\right\} \tag{4}$$

$$\eta = \phi_S - \phi_E - E^0 \tag{5}$$

Here, k is the reaction rate coefficient, ϵ^* is the normalized volume fraction ($0 < \epsilon^* < 1$) of solid species in the electrode, E^0 is the reaction's standard potential vs Li/Li^+, η is the overpotential, and β is the symmetry factor for the reactions. The normalized volume

https://doi.org/10.1021/acsami.5c20956
ACS Appl. Mater. Interfaces 2026, 18, 1626−1640

Table 1. Reaction Processes and Corresponding Equilibrium Potentials (in V vs. Li/Li^+) for Sulfur, FeS_2 and FeF_3 Electrodes Based on Previous Studies[33,57,60,65,66]

reaction	E^0	reaction	E^0
sulfur			
lithiation		**delithiation**	
$S_8 + 8Li^+ + 8e^- \rightarrow 4Li_2S_2$ (R1)	2.1	$8Li_2S \rightarrow 16Li^+ + 16e^- + S_8$ (R3)	2.7
$Li_2S_2 + 2Li^+ + 2e^- \rightarrow 2Li_2S$ (R2)	2.05		
FeS_2			
initial lithiation		**delithiation**	
$FeS_2 + 4Li^+ + 4e^- \rightarrow 2Li_2S + Fe$ (R4)	1.85	$Fe + Li_2S \rightarrow FeS + 2Li^+ + 2e^-$ (R7)	1.8
		$8Li_2S \rightarrow S_8 + 16Li^+ + 16e^-$ (R8)	2.4
subsequent lithiation steps			
$FeS + 2xLi^+ + 2xe^- \rightarrow Li_{2x}FeS$ (R5)	2.2		
$Li_{2x}FeS + (2-2x)Li^+ + (2-2x)e^- \rightarrow Fe + Li_2S$ (R6)	1.4		
FeF_3			
lithiation		**delithiation**	
$FeF_3 + Li^+ + e^- \rightarrow LiFeF_3$ (R9)	2.2	$Fe + 3LiF \rightarrow LiFeF_3 + 2Li^+ + 2e^-$ (R11)	2.0
$LiFeF_3 + 2Li^+ + 2e^- \rightarrow Fe + 3LiF$ (R10)	1.8	$LiFeF_3 \rightarrow FeF_3 + Li^+ + e^-$ (R12)	2.6

fraction is calculated by dividing the species volume fraction with the initial volume fraction. As the reaction proceeds, the rate of consumption and generation of species can be given as shown in eqs 6 and 7:

$$\frac{\partial \varepsilon_A}{\partial t} = -\frac{a_s i}{nF} V_A \quad (6)$$

$$\frac{\partial \varepsilon_B}{\partial t} = \frac{a_s i}{nF} V_B \quad (7)$$

Here, V_i is the molar volume of the species, a_s is the specific active area, and n is the number of electrons transferred during the reaction.

The volume expansion (%) of the cathode is calculated as eq 8:

$$\Delta V = \frac{(\sum_1^n V_i c_i)_{final} - (\sum_1^n V_i c_i)_{initial}}{(\sum_1^n V_i c_i)_{initial}} \times 100 \quad (8)$$

As a first approximation, we assume that the volume change does not alter the electrode microstructural properties.

RESULTS AND DISCUSSION

Electrochemical Behavior

The electrochemical behavior of sulfur, FeS_2, and FeF_3 electrode composites was investigated at room temperature in anvil-type solid-state cells. These cells were cycled at a constant current density of 0.1 mA cm^{-2} between 1.4 and 3.0 V vs. Li/Li^+, they featured a stack pressure of 20 MPa, they used an argyrodite-type Li_6PS_5Cl (LPSC) solid electrolyte, and they contained a 20-μm thick lithium foil counter electrode. The cathode active material (CAM) loading corresponded to an areal capacity of 4.0 mAh cm^{-2}. The lithiation-delithiation profiles (Figure 1a–c) show distinct behavior for each active material. The sulfur cathode (Figure 1a) achieved an areal capacity of 1.7 mAh cm^{-2} upon initial lithiation, equivalent to a specific capacity of 675 mAh g_{sulfur}^{-1}. This is only 42.5% of the theoretical capacity; this relatively low capacity is expected for sulfur cathodes operated at room temperature without structural or morphological modifications and moderate stack pressures. In other studies, stack pressures for these types of cells have varied between 50 to a few hundred MPa.[12,30,48,50,57,58] In comparison, FeS_2 and FeF_3 demonstrated higher initial areal lithiation (discharge) capacities of 2.5 and 2.0 mAh cm^{-2}, respectively, with corresponding specific capacities of 628 mAh $g_{FeS_2}^{-1}$ and 535 mAh $g_{FeF_3}^{-1}$ (Figure 1b,c). Both FeS_2 and FeF_3 exhibit higher fractional capacity of theoretical compared to the sulfur composite (70.5% and 75.2%, respectively). Similar cells cycled with $LiNi_{0.6}Mn_{0.2}Co_{0.2}O_2$ (NMC622) counter electrodes exhibited slightly higher initial specific capacities of 855 mAh g_{sulfur}^{-1}, 697 mAh $g_{FeS_2}^{-1}$, and 695 mAh $g_{FeF_3}^{-1}$, which could be attributed to better interfacial contact between the Li_6PS_5Cl separator and the counter electrode during the application of formation pressure and densification of composites[59] (Figure S1).

The dQ/dV curves derived from the sulfur composite data (Figure 1d) provide detailed insights into the redox reactions during the initial lithiation and subsequent first full cycle. The initial lithiation dQ/dV curve from the sulfur composite shows a similar shape compared to the following lithiation. A broad discharge peak with two small features at 1.95 and 2.05 V is observed in both discharges, while the peak at 2.05 V is more pronounced in the initial lithiation likely due to activation of sulfur and surface reconstruction.[25] The peak located at 2.05 V is attributed to the reduction of sulfur to Li_2S_2, while the second corresponds to the formation of the final lithiation product (Li_2S), although these processes are likely overlapping.

The cells containing FeS_2 and FeF_3 electrodes show greater differences in their voltage profiles between the initial lithiation and the following cycle, which reflects chemical and structural changes during the initial conversion reaction upon lithiation (Figure 1b,c and e,f). For FeS_2, the peak in the dQ/dV data at ca. 1.55 V represents the conversion of FeS_2 to Li_2S and metallic iron species. During the first delithiation, two peaks appear at 1.8 and 2.4 V. The first peak is attributed to the reaction between metallic iron and Li_2S, forming FeS, while the second involves conversion of Li_2S to sulfur (Figure 1e). The FeF_3 cell features one peak at 2.25 V during the initial lithiation, attributed to the intercalation of lithium into FeF_3, followed by the formation of $LiFeF_3$ (Figure 1f). A conversion reaction occurs at 1.8 V, which leads to the formation of LiF and metallic iron species (Table 1).[60]

https://doi.org/10.1021/acsami.5c20956
ACS Appl. Mater. Interfaces 2026, 18, 1626–1640

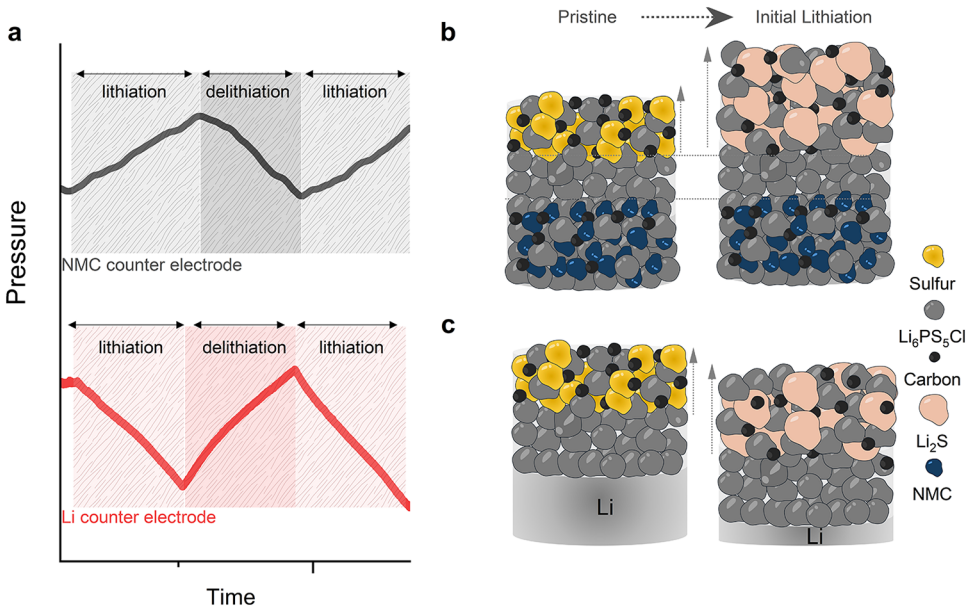

Figure 2. Pressure evolution in cells with conversion cathodes with different counter electrodes. (a) Typical experimental data in a constant-volume cell showing pressure change during lithiation, delithiation, and second lithiation when using composite conversion cathodes paired with different counter electrodes: NMC622 counter electrode (black) and lithium metal counter electrode (red). (b–c) Schematics of the volume changes of the cell stacks with (b) NMC622 and (c) lithium counter electrodes. The balance of the partial molar volume of lithium species in each electrode determines the net volume change, with a net increase in stack volume (increasing stack pressure) during lithiation when using an NMC622 counter electrode and a net decrease in stack volume (decreasing stack pressure) during lithiation when using a lithium counter electrode.

Stack Pressure Evolution

The selection of these three conversion materials was motivated by their distinct conversion reactions during initial lithiation, as demonstrated in Figure 1. These different reactions involve varying volume changes. FeF_3 undergoes an initial intercalation reaction followed by a two-electron conversion reaction, with a volume increase of 25% during the full lithiation process.[60] In contrast, the conversion of S_8 to $8Li_2S$ involves a 16-electron transfer reaction and generally occurs as a two-step reaction, which includes the formation of a metastable Li_2S_2 phase followed by conversion to the Li_2S phase, resulting in a volume increase of 80%.[28] FeS_2 undergoes a two-step, four-electron transfer reaction during the initial lithiation, leading to a substantial volume increase of 159%.[29]

To examine how electrochemical behavior is linked to stack pressure evolution and volume changes in these conversion cathodes, a custom solid-state cell assembly with an integrated force sensor was used (see Experimental section). This cell approximates a constant volume environment, with the polyether ether ketone (PEEK) casing and metal rods held in place without springs and the force sensor measuring changes in force due to volume changes of the active materials. Cells with sulfur, FeS_2, or FeF_3 composite electrodes were used with either lithium or NMC622 counter electrodes (Figure 2).[39]

Figure 2 depicts the distinct volume change and stack pressure evolution behaviors of these conversion electrode materials when paired with different counter electrodes. When lithium metal is used as the counter electrode, its large volume changes during cycling due to the high molar volume of Li dominate the overall pressure evolution,[52,61] effectively masking pressure contributions from the conversion cathode composite (Figure 2a). As a result, the overall stack pressure decreases during lithiation due to the net volume decrease of the cell stack (Figure 2c), and the greater volume change of Li compared to the conversion cathode makes it difficult to isolate the individual contributions of the cathode composite from the overall stack pressure change. In contrast, using an intercalation-type material as the counter electrode allows for the conversion cathode to play a greater role in the net stack volume evolution. Intercalation materials feature smaller partial molar volumes of Li^+ and thus undergo smaller volume changes (typically in the range of 2–5%) compared to lithium metal.[62] This reduced volume change minimizes the impact of the counter electrode on the overall pressure evolution, allowing the chemo-mechanical behavior of the conversion cathode composites to be more clearly observed and studied (Figure 2b). The pressure evolution in these cells is thus predominantly governed by the conversion cathode, as the counter electrode contribution is minimized. As shown in Figure 2a, this results in a net pressure increase during lithiation due to the net volume change of the stack being controlled by the conversion cathode, which expands upon lithiation. The cell configuration with an NMC622 counter electrode allows for more detailed investigation of pressure-reaction linkages for the conversion cathode, and the overall trends in Figure 2 highlight the need to consider the (partial) molar volume balance of Li species within the electrodes in determining volume changes and pressure evolution.

The experimental results in Figure 3a–c show voltage traces (top) and measured stack pressure changes (bottom) over three cycles for cells containing sulfur (Figure 3a), FeS_2 (Figure 3b), and FeF_3 (Figure 3c), along with 20-μm thick Li metal counter electrodes. The initial stack pressure was set to approximately 21 MPa. In all cases, the stack pressure evolution during cycling exhibits a clear cyclic pattern, in which it decreases during lithiation of the active material and increases during delithiation, which reflects the net volume contraction of the stack upon lithiation of the cathode and net volume expansion of the stack during delithiation (as shown in

https://doi.org/10.1021/acsami.5c20956
ACS Appl. Mater. Interfaces 2026, 18, 1626–1640

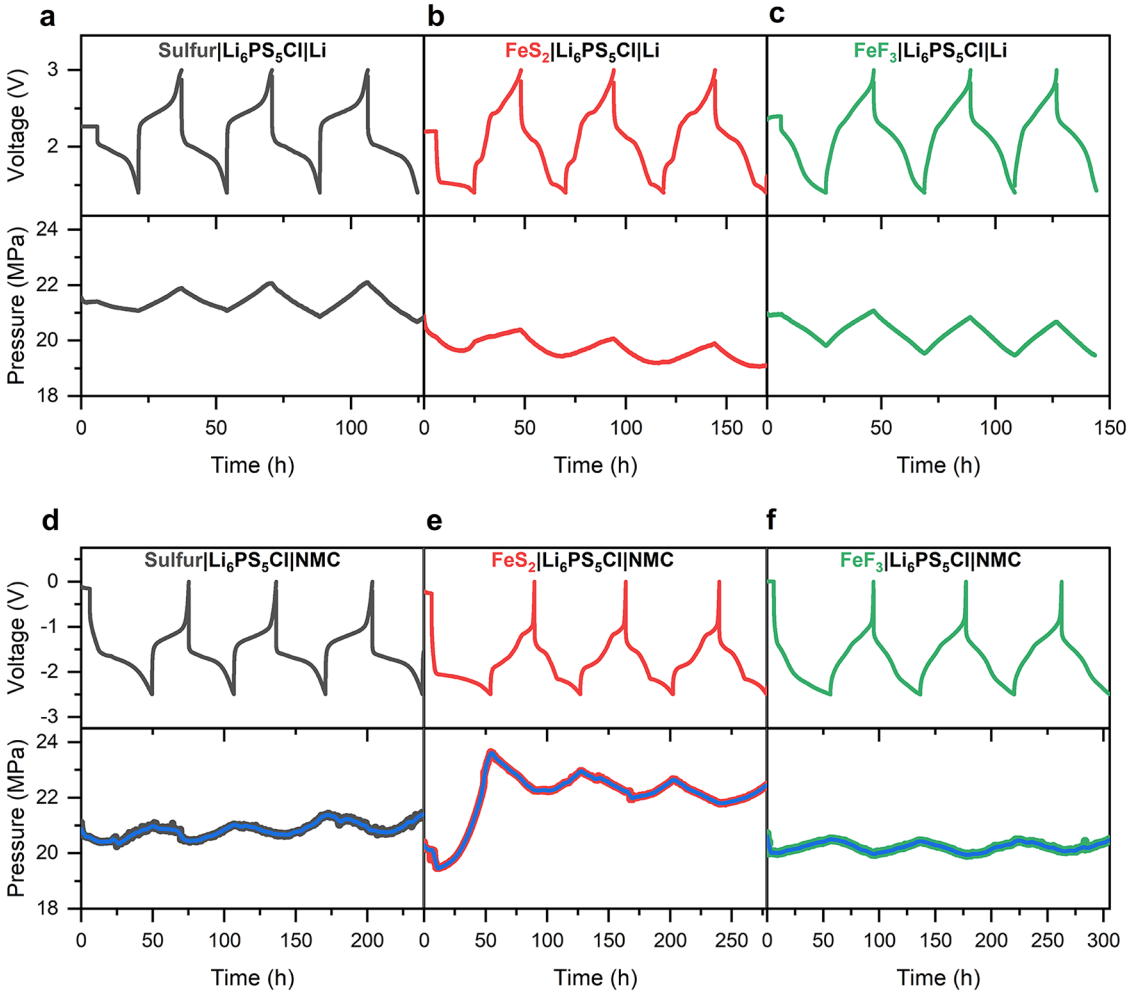

Figure 3. Galvanostatic voltage profiles (top) coupled with in situ stack pressure measurements (bottom) of composite conversion material working electrodes with different counter electrodes in solid-state cells with Li_6PS_5Cl solid electrolyte. (a–c) Sulfur (a), FeS_2 (b), and FeF_3 (c) composite working electrodes in cells with 20 μm-thick Li negative electrodes. (d–f) Sulfur (d), FeS_2 (e), and FeF_3 (f) composite working electrodes in cells with NMC622 composite counter electrodes. The blue lines are smoothened using a Savitzky-Golay filter. Each cell was tested with a current density of 0.1 mA cm^{-2} at 25 °C.

Figure 2). This behavior is consistent across the three materials, although the magnitudes and shapes of the pressure responses vary due to differences in reaction mechanisms and volume change characteristics (to be discussed subsequently). The cell with FeF_3 exhibited the greatest pressure changes, with a 1.1 MPa decrease during initial lithiation, while the cell with FeS_2 showed the lowest (0.6 MPa).

The cells cycled with NMC622 counter electrodes (Figure 3d–f) show pressure evolution trends that are opposite to those observed with a lithium metal counter electrode; specifically, there is an increase in stack pressure during lithiation and a decrease during delithiation. The cell with a sulfur electrode shows a 0.8 MPa stack pressure increase during the first lithiation (Figure 3d). There were slightly higher pressure changes for sulfur in the following cycles due to higher capacity in later cycles related to activation of additional sulfur.[63] FeS_2 exhibits a substantial stack pressure increase of about 4 MPa during the initial lithiation, followed by smaller (~1 MPa) cyclic pressure changes at higher stack pressure during cycling (Figure 3e). The large pressure change on the first lithiation indicates much larger volume change and a distinct conversion reaction pathway on the first discharge compared to further cycling. This finding is related to the different electrochemical signatures during the first vs. later lithiation processes for FeS_2 (Figures 1b and 3e), suggesting different reaction pathways. Interestingly, the FeS_2 cell with a lithium counter electrode (Figure 3b) shows only a minimal pressure change on the first lithiation, indicating that the volume expansion of the FeS_2 electrode is mostly negated by the contraction of the lithium counter electrode. The cell with a FeF_3 working electrode and NMC counter electrode shows a cyclic stack pressure change of ~0.5 MPa (Figure 3f). Finally, it should be noted that the magnitude of pressure change is dependent on the initial stack pressure values as well as the details of the cell assembly and configuration, and differences are therefore expected when comparing these magnitudes to other studies. For instance, Lee et al. observed approximately 4 MPa change in pressure with 70 MPa applied stack pressure for a sulfur cathode.[50] However, direct comparison of the different materials within the current study using identical cell configurations provides useful insight.

Pressure Hysteresis and Slope

Figure 4a presents the stack pressure evolution as a function of normalized capacity for cells with sulfur, FeS_2, and FeF_3 cathodes in the first and third cycles using Li metal counter

https://doi.org/10.1021/acsami.5c20956
ACS Appl. Mater. Interfaces 2026, 18, 1626–1640

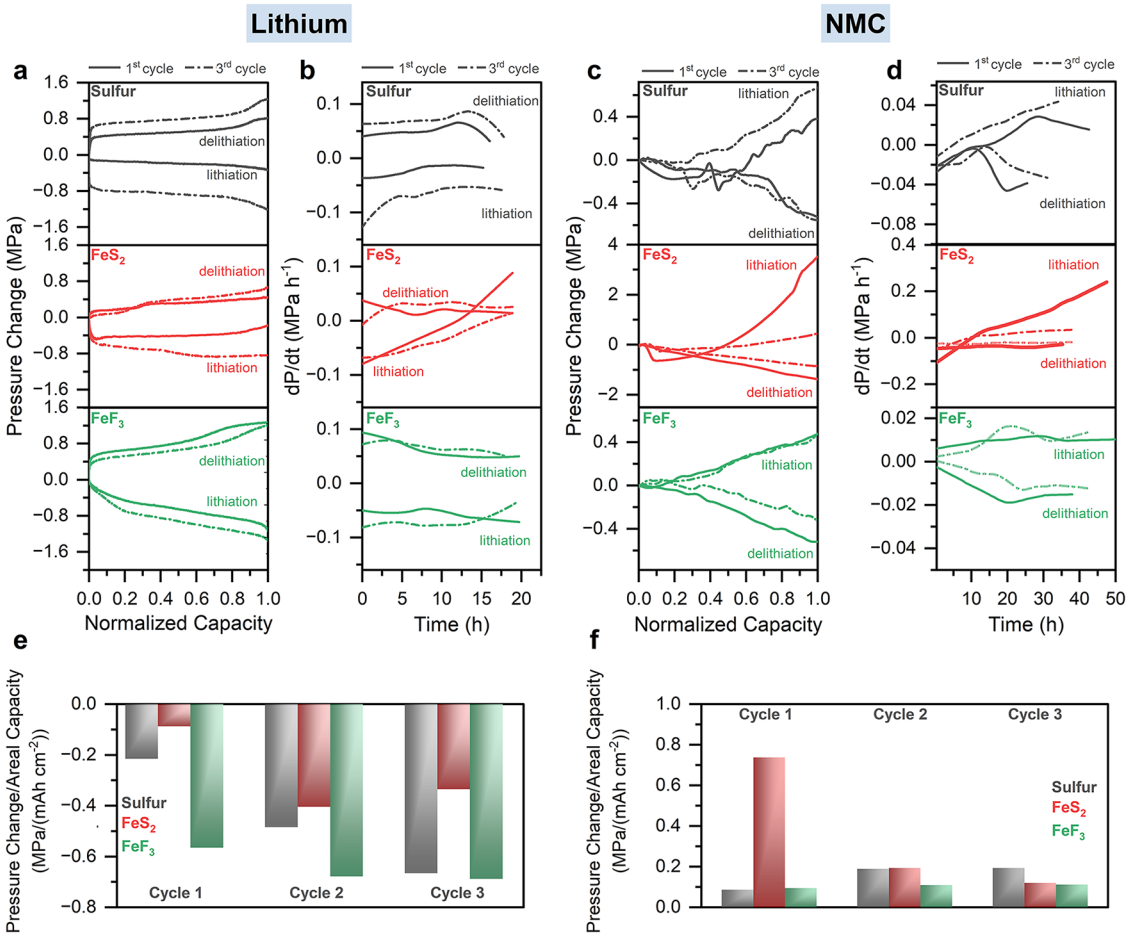

Figure 4. Pressure hysteresis and dP/dt analysis during cell cycling. (a) Stack pressure changes of cells featuring the composite conversion electrodes with lithium counter electrodes with respect to capacity normalized by the maximum capacity and (b) corresponding differential analysis (dP/dt curves) of the stack pressure evolution of cells with sulfur (**top**), FeS_2 (**middle**), and FeF_3 (**bottom**). (c) Stack pressure changes of cells featuring the composite conversion electrodes with NMC counter electrodes with respect to capacity normalized by the maximum capacity and (d) corresponding differential analysis (dP/dt curves) of the stack pressure evolution of cells with sulfur (**top**), FeS_2 (**middle**), and FeF_3 (**bottom**). Stack pressure change normalized by the areal capacity of the cells over the first three cycles for sulfur (gray), FeS_2 (red), and FeF_3 (green) in cells with lithium counter electrodes (e) and NMC counter electrodes (f).

electrodes. A 20-μm lithium film on Cu was used to avoid excess flow of thicker Li foils under stack pressure, and it avoids phase inhomogeneities often observed with lithium–indium alloy counter electrodes.[51,64] During the first cycle, the sulfur and FeS_2 cathodes show smaller variations in stack pressure than FeF_3. This is likely because FeF_3 undergoes the smallest intrinsic volume change among the three cathodes during its conversion reaction, making the overall stack pressure more strongly influenced by the large volume changes of the lithium counter electrode, which dominate pressure evolution of the cell stack. By the third cycle, both sulfur and FeS_2 show higher stack pressure changes compared to the first cycle, which can be attributed to the gradual activation and improved electrochemical utilization of these materials. In all three systems, the slope of the pressure response changes as capacity increases, particularly toward the end of lithiation.

Figure 4b shows the corresponding time derivatives of the stack pressure (dP/dt) for each of the conversion cathode cells in Figure 4a. The dP/dt curves provide insight into how lithiation and delithiation dynamics evolve over time. They can also reveal changes of the effective partial molar volume during half-reactions since the time axis is a proxy for charge passed in these galvanostatic experiments. Previous studies on silicon[38] and graphite[42] anodes have correlated stack pressure changes to structural evolution of the electrodes by using such dP/dt analysis during electrochemical cycling.

The dP/dt curves of cells containing sulfur, FeS_2 and FeF_3 electrodes with Li counter electrodes (Figure 4b) show that the slopes of the pressure changes are not necessarily constant throughout the lithiation/delithiation processes. Similar non-constant behavior is observed for the materials when using NMC counter electrodes (Figure 4c,d). Varying dP/dt values indicate that the volume change varies with state of charge (SOC). This can be due to SOC-dependent partial molar volume of Li ($\overline{V_m}$) within the conversion material, or to the effects of porosity within the composite electrode that can accommodate some of the expanding volume and therefore reduce the exerted force. Of note, the cell with the FeS_2 working electrode and NMC counter electrode (Figure 4d) exhibited a substantial (~4 MPa) pressure increase during the first lithiation, with the dP/dt curve also continuously increasing during the lithiation. There is a significant volume expansion of the FeS_2 cathode during this first lithiation, which is then lessened on subsequent cycling. Since this is a continuous conversion reaction to form Li_2S and metallic iron particles with theoretically constant $\overline{V_m}$, the increasing

https://doi.org/10.1021/acsami.5c20956
ACS Appl. Mater. Interfaces 2026, 18, 1626−1640

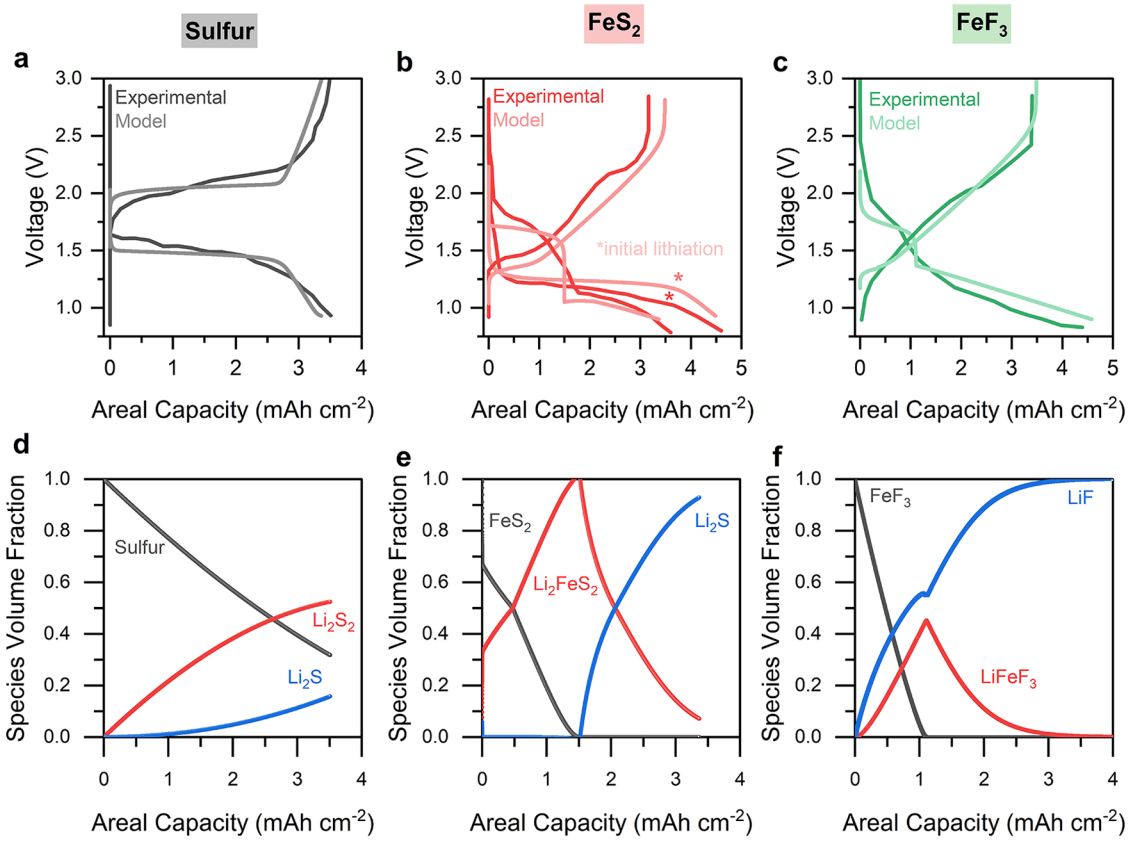

Figure 5. Comparison of the electrochemical behavior predicted by the model with experimental data for cells with (a) sulfur, (b) FeS_2, and (c) FeF_3 cathodes during both lithiation and delithiation processes. Two discharge curves (initial lithiation and first cycle) are highlighted for the FeS_2 cathode demonstrating disparate reaction pathways after the first cycle. Consumption and generation of different phases during the lithiation process for (d) sulfur, (e) FeS_2, and (f) FeF_3 cathodes.

slope with lithiation suggests that the expanding volume progressively fills pores within the composite, gradually exerting higher forces as the pores are filled. Furthermore, the initially negative dP/dt of the sulfur composite during lithiation (Figure 4c,d) also suggests pore filling during initial expansion, which may be due to highly distributed sulfur within the composite electrode. In contrast, FeF_3 features positive dP/dt values during lithiation, indicating that the lithiation-induced expansion directly translates into measured stack pressure. These findings emphasize the complex interplay between microstructural changes and partial molar volume ($\overline{V_m}$) variations in determining the internal pressure evolution within SSBs.

Analysis of the stack pressure normalized by the areal capacity of the cells, both with lithium counter electrodes (Figure 4e) and NMC counter electrodes (Figure 4f), allows for comparisons of overall stack pressure evolution while removing differences in specific capacity of the cells. With lithium counter electrodes (Figure 4e), the cells with FeF_3 electrodes show the largest normalized stack pressure changes over each cycle, which is likely due to the dominant contribution of the lithium counter electrode with FeF_3 featuring relatively low volume change. The increase in the pressure change to areal capacity ratio from after the first cycle likely arises from progressive mechanical and electrochemical activation. During the first cycle, redistribution of reaction products or improved Li^+ accessibility could increase the fraction of material participating in (de)lithiation, leading to larger volume changes per unit capacity. With NMC counter electrodes (Figure 4f), the large normalized pressure change of the FeS_2 in the first cycle is notable, which is reduced on later cycles.

Microkinetic Modeling

To investigate the species evolution and reaction kinetics in solid-state conversion cathodes, we developed a mechanistic modeling framework to capture the electrode-scale reactions, transport processes, and electrochemical response of the cell. The electrochemical performance of the cell is strongly influenced by the physicochemical interactions and species evolution associated with the electrochemical reactions. Given the distinct active materials (sulfur, FeS_2, and FeF_3), the different species generated during each reaction lead to varying performance characteristics. The modeling framework couples reaction kinetics, charge transport, species evolution, and surface passivation arising from the formation of insulating Li_2S and LiF, which restricts both ionic and electronic transport and impedes reaction reversibility. Butler–Volmer kinetics is used to capture the lithiation and delithiation behavior of the cells. The electrode microstructure is assumed to remain fixed during discharge, and the chemo-mechanical effects arising from volume changes associated with phase conversion are not included in the model. These coupled deformation driven effects remain an important direction for future work. The details of the model are explained in the Experimental section.

Based on previously reported studies,[33,57,60,65,66] the reactions shown in Table 1 and their corresponding

https://doi.org/10.1021/acsami.5c20956
ACS Appl. Mater. Interfaces 2026, 18, 1626−1640

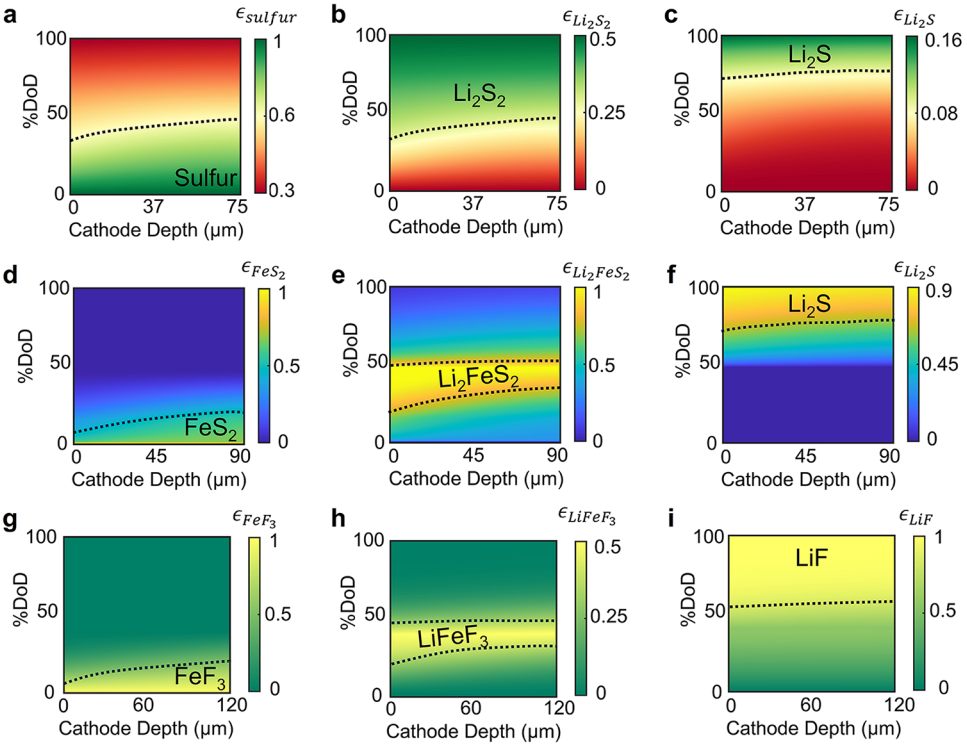

Figure 6. Spatiotemporal evolution of species in (a–c) sulfur, (d–f) FeS_2, and (g–i) FeF_3 composite cathodes as a function of depth of discharge (DoD). Here, the vertical axis tracks lithiation progression, the horizontal axis denotes cathode depth, and ϵ_i denotes the volume fraction of species *i*.

equilibrium potentials (vs Li/Li^+) are assumed to occur in the cathode during lithiation and delithiation in the various cases considered in the model.

A comprehensive validation of the proposed model was conducted for all three cathode chemistries during both lithiation and delithiation processes at a current density of 0.1 mA cm^{-2}, as illustrated in Figure 5a–c. These plots contain experimental data as well as simulated data from our model. The predicted voltage curves from the model demonstrate excellent agreement with the experimental curves, with similar voltage features corresponding to the various phase transitions, as well as similar reaction overpotentials.

Reactions R1 and R2 (Table 1) depict the lithiation reaction pathway in a typical solid-state sulfur cathode, where Li_2S_2 forms as an intermediate during the conversion of elemental sulfur to Li_2S.[57] The close proximity of the equilibrium potentials for these reactions results in a spectrum of coexistence between Li_2S_2 and Li_2S throughout the lithiation process. Figure 5d shows the phases present (as predicted by the model and based on the voltage curve) during lithiation. This plot illustrates that at the initial stage of lithiation, sulfur converts predominantly to Li_2S_2, with only minor Li_2S formation. As lithiation progresses, Li_2S_2 further reacts to form Li_2S (Figure S2). However, Li_2S, being an electronic insulator, forms a passivating layer on the sulfur surface that obstructs electron percolation within the active material. As a result, 31.7% of sulfur remains unreacted, while only 15.8% is converted to Li_2S and 52.5% to Li_2S_2. The buildup of Li_2S leads to increased overpotentials and a characteristic voltage drop (Figure 1a), reflecting the kinetic hindrance imposed by the insulating lithiation (discharge) product.

However, the FeS_2 and FeF_3 cathodes exhibit distinct species evolution behavior during lithiation. In FeS_2 cathodes, the significant difference between the equilibrium potentials of the two reactions results in FeS_2 being fully converted to Li_2FeS_2 before Li_2FeS_2 is subsequently transformed into Li_2S to complete the lithiation reaction (Figure 5e). In the FeF_3 cathode, FeF_3 is initially converted to $LiFeF_3$, and due to the relatively small equilibrium potential difference with the second reaction, $LiFeF_3$ simultaneously converts to LiF during the lithiation process (Figure 5f). Although Li_2S also forms during FeS_2 conversion, and LiF in the case of FeF_3 exhibits similar insulating behavior, the concurrent *in situ* formation of metallic Fe in both of these cases provides electronic pathways that sustain reaction front propagation. This mechanism enables more complete conversion of FeS_2 and FeF_3, resulting in a higher percentage of active material utilization compared to the sulfur cathode (Figure 5e,f).

The distinct electrochemical characteristics of the active materials and their lithiation products dictate the extent of active material consumption and the spatial evolution of species within the electrode (Figure 6). To ensure consistent areal capacity, the electrode thicknesses were set to 75 μm for sulfur, 90 μm for FeS_2, and 120 μm for FeF_3. Across all three cathode chemistries, the lithiation process induces moderate concentration gradients, primarily due to the limited transport of Li^+ ions through solid–solid contact interfaces within the composite electrode. Unlike liquid electrolytes, where ion transport is rapid and spatially uniform, solid-state systems rely on point or surface contacts between particles for ion conduction. This restricted transport confines lithiation predominantly to regions adjacent to the separator–cathode interface, where lithium availability is highest. As lithiation of the active material progresses, the reaction front gradually advances inward as ionic accessibility permits, leading to a spatially resolved reaction zone within the cathode.[67,68]

https://doi.org/10.1021/acsami.5c20956
ACS Appl. Mater. Interfaces 2026, 18, 1626–1640

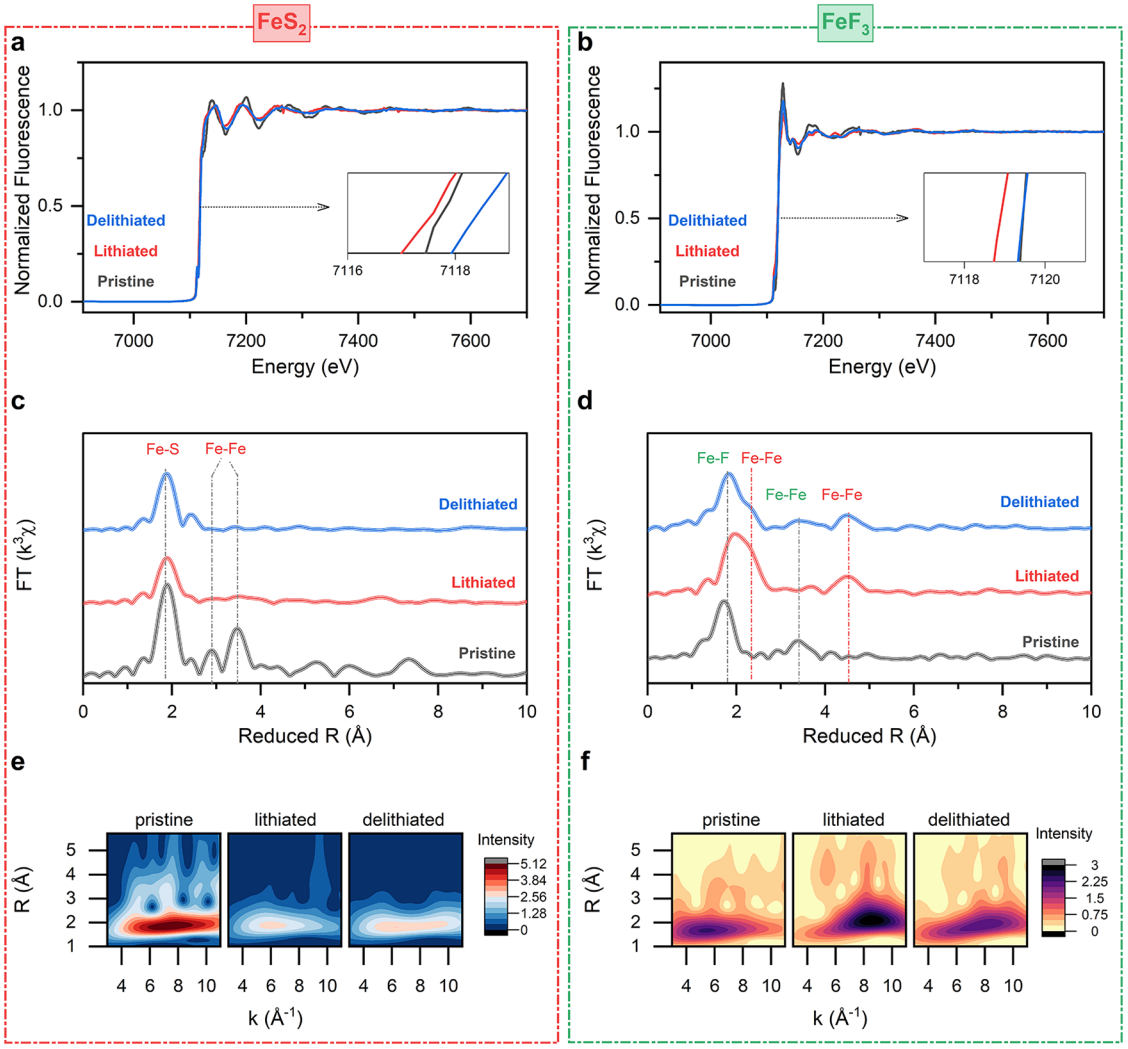

Figure 7. Ex situ X-ray absorption spectroscopy analysis of FeS_2 and FeF_3 composites. Fe K-edge X-ray absorption near-edge (XANES) spectra of (a) FeS_2 and (b) FeF_3. Extended X-ray absorption fine-structure of (c) FeS_2 and (d) FeF_3 composite cathodes. WT-EXAFS of (e) FeS_2 and (f) FeF_3 composite cathodes in the pristine state (black), after the initial lithiation (red) and after the first delithiation (blue).

Interestingly, the initial concentration gradients diminish across all three cathode systems toward the end of the lithiation (Figure 6). This homogenization arises from the progressive deactivation of reaction sites near the separator interface by insulating lithiation products, such as Li_2S or LiF, which impede further electrochemical reactions at these locations. As a result, the current density redistributes toward deeper regions of the electrode that remain electrochemically active. This redistribution promotes the advancement of the lithiation front until the remaining unreacted material becomes limited by ionic transport or is passivated by insulating phases. Consequently, the lithiation process transitions from being reaction-kinetics-controlled at the interface to being transport-limited within the electrode bulk.

The differing molar volumes and fractions of active materials and lithiation products give rise to distinct degrees of cathode expansion, governed by both reaction stoichiometry and the physical properties of the phases involved. We estimate the extent of expansion by combining the molar volume and species fraction of each phase, assuming constant microstructural properties and cathode thickness during volume change (See Experimental section). In the sulfur cathode,[19] the molar volumes of Li_2S_2 and Li_2S are approximately 60 and 80% greater than that of sulfur, respectively, leading to a 26% increase in cathode volume by the end of lithiation due to mixed product formation (Figure S3). FeS_2 exhibits the highest expansion (110%), followed by sulfur (26%) and FeF_3 (21%), reflecting variations in both product volumes and conversion extents.

These results suggest that volume expansion is not merely a mechanical effect but a critical factor that could influence interfacial contact, reaction front propagation, and electrochemical performance. Therefore, understanding and managing cathode expansion remains essential for the design of stable and high-performance solid-state conversion cathodes. Since solid−solid contact area and cathode thickness inevitably evolve with expansion and contraction, accounting for microstructural changes is a critical direction for future work.

We next investigated the morphological evolution of cathode composites using cross-sectional scanning electron microscopy (SEM) to assess crack formation, void development, and delamination (Figures S4−5). Initially, all pristine pellets exhibited compact and dense microstructures (Figure S4). However, after one electrochemical cycle, degradation was observed across all samples, including cracking and delamination. This degradation is primarily attributed to the large

https://doi.org/10.1021/acsami.5c20956
ACS Appl. Mater. Interfaces 2026, 18, 1626−1640

volume changes associated with conversion-type reactions during lithiation and delithiation. The severity of these structural changes underscores the mechanical instability of these cathode materials under realistic operating conditions. Moreover, the complex reaction pathways of these materials, often involving multiple intermediate phases, may contribute to nonuniform expansion, further exacerbating the mechanical stress. The magnified SEM images of the pristine and delithiated state of the various cathode composites are shown in Figure S5, showing that all undergo morphology changes after one cycle.

X-ray Absorption Spectroscopy

In comparison to sulfur, the reaction mechanisms of FeS_2 and FeF_3 are complicated by the chemo-mechanical interactions of iron species with the lithium−sulfur species, as well as the formation of a variety of reaction intermediates and products during cycling.[13,69,70] To analyze the formation of iron species with different oxidation states, we performed *ex situ* XAFS measurements at the Fe K-edge for FeS_2 and FeF_3 electrode composites using pristine, lithiated and delithiated pellets (Figure 7). The X-ray absorption near edge structure (XANES) region captures the valency and electronic configuration of the iron species. The Fe K-edge positions were determined using the half-height method (Table S1), where the edge is defined as the energy at which the normalized absorption reaches 50% of the maximum intensity (Figure 7a,b, insets). For FeS_2, the edge shifts slightly to lower energy in the lithiated state, indicating the formation of Li_2FeS_2 with Fe^{2+} as well as metallic iron particles.[71] It is known that FeS_2 tends to form nanoscale metallic iron particles at the end of discharge, which may explain the absence of distinct Fe shells in the R-space spectrum.[72] Upon delithiation, the edge shifts slightly to higher energy, suggesting the formation of species different from the initial FeS_2, consistent with electrokinetic modeling and confirming the formation of FeS. While both FeS_2 and FeS contain Fe^{2+}, their electronic structures differ substantially.[73] The FeF_3 material exhibits different behavior. The lower Fe K-edge of FeF_3 is attributed to the reaction between FeF_3 and Li_6PS_5Cl that promotes formation of FeS that shifts the K-edge to the lower energy range.[15,74] The Fe K-edge shifts by approximately 0.5 eV to lower energy upon discharge, confirming lithiation. After charging, the edge returns to its original position, indicating reversible delithiation.

Fourier-transformed (Figures 7c,d and S6−7) and wavelet-transformed (Figure 7e,f) extended X-ray absorption fine structure (EXAFS) spectra for FeS_2 and FeF_3 reveal distinct coordination environments across different states of charge. Fitting of the Fourier-transformed spectra confirms the presence of Li_2FeS_2 even at the end of the first lithiation reaction and the formation of FeS after delithiation. In FeF_3, changes in Fe−F coordination are observed around 2 Å, along with the appearance of new coordination shells near 4.3 Å, indicative of metallic iron formation.[75] The irreversible chemical evolution of FeS_2 correlates with the asymmetric pressure hysteresis observed during cycling. Such irreversible phase transitions generate internal stress and contribute to chemo-mechanical degradation. In contrast, these measurements show that FeF_3 exhibits more reversible redox processes, and it is reflected in the relatively symmetric cyclic pressure profiles that suggest less structural disruption and lower residual stress accumulation. Wavelet-transformed EXAFS (WT-EXAFS) provides a two-dimensional representation of the EXAFS signal in both *R* and *k* space, allowing the separation of overlapping scattering paths and enabling the identification of different neighboring atoms that are otherwise indistinguishable in conventional Fourier-transformed spectra. The WT spectra of both FeS_2 (Figure 7e) and FeF_3 (Figure 7f) display clear variations in energy space, reflecting changes in the local coordination environment of iron sites during cycling. We note that the *ex situ* XAS measurements presented here capture only the final reaction states after full lithiation or delithiation and therefore cannot directly resolve transient intermediate phases that may form during cycling. Nevertheless, the presence and evolution of such intermediates can be inferred through a combination of electrochemical signatures, stack pressure evolution, and observed mechanistic pathways reported in prior studies.[60,65,66] Specifically, the nonlinear and stepwise pressure changes observed during the early stages of lithiation are consistent with sequential phase evolution. Future *in situ* XAS or *operando* diffraction studies would further resolve the real-time evolution of these phases and provide direct validation of the inferred mechanisms.

CONCLUSIONS

This study investigates the electro-chemo-mechanical behavior of sulfur, FeS_2, and FeF_3 conversion cathode composites in solid-state batteries. These materials undergo varying degrees of volume expansion and contraction during cycling. We demonstrate that volume changes in the counter electrode can significantly influence the overall volume evolution of the cell stack. All three cathodes exhibit pressure profiles with changing slopes during lithiation and delithiation, varying across cycles. Our findings link pressure changes to the formation of reaction intermediate and final products via microkinetic modeling, correlating these with microstructural evolution. Spectroscopic analyses reveal that FeS_2 and FeF_3 possess distinct iron coordination environments, resulting in characteristic differences in their microstructural transformations.

This work establishes a connection between microstructural evolution and the chemo-mechanical behavior of these materials. Looking forward, further investigation of the reaction mechanisms, along with *operando* imaging and spectroscopy, is essential to fully understand and address the chemo-mechanical challenges in these systems. Investigation at reduced stack pressures is also necessary, as this is relevant to practical devices. Low stack pressures may exacerbate loss of interparticle contact and accelerate capacity fade, particularly if electrode porosity is not carefully optimized. Porous architecture of the composite cathodes can help accommodate volume fluctuations but must balance mechanical properties and ionic and/or electronic transport pathways. Understanding the interplay between volume change, porosity, and stack pressure is key for designing stable, high-capacity conversion-type cathodes for solid-state batteries.

ASSOCIATED CONTENT

Data Availability Statement

All data of this study are available from the corresponding author upon reasonable request.

Supporting Information

The Supporting Information is available free of charge at https://pubs.acs.org/doi/10.1021/acsami.5c20956.

https://doi.org/10.1021/acsami.5c20956
ACS Appl. Mater. Interfaces 2026, 18, 1626−1640

XANES and EXAFS modeling results. Supporting figures include **Supporting Figure S1**. Electrochemical behavior of sulfur, FeS_2, and FeF_3 cathodes cycled with NMC counter electrodes. **Figure S2**. Microstructural evolution during discharge. The left panel shows the initial stage where sulfur begins to convert to Li_2S_2. The middle panel corresponds to an intermediate state where sulfur is partially converted to Li_2S_2 and Li_2S_2 begins transitioning to Li_2S. The right panel represents the discharged state containing a mixed Li_2S_2 and Li_2S product distribution. **Figure S3**. Volume expansion for sulfur, FeS_2 and FeF_3 cathodes during the lithiation process. **Figures S4−5**. SEM images of pristine electrodes (a-c) and electrodes after one cycle (in the delithiated state) (d-f) of sulfur, FeS_2, and FeF_3 cathodes, respectively. **Figure S6**. k-space X-ray absorption fine-structure spectra of FeS_2in the pristine, discharged, and charged states at the Fe K-edge. **Figure S7**. k-space X-ray absorption fine-structure spectra of FeF_3 in the pristine, discharged, and charged states at the Fe K-edge. (PDF)

AUTHOR INFORMATION

Corresponding Author

Matthew T. McDowell − *George W. Woodruff School of Mechanical Engineering, Georgia Institute of Technology, Atlanta, Georgia 30332, United States; School of Materials Science and Engineering, Georgia Institute of Technology, Atlanta, Georgia 30332, United States;* orcid.org/0000-0001-5552-3456; Email: mattmcdowell@gatech.edu

Authors

Elif Pınar Alsaç − *George W. Woodruff School of Mechanical Engineering, Georgia Institute of Technology, Atlanta, Georgia 30332, United States;* orcid.org/0000-0002-4255-9676

Arpan Kumar Sharma − *School of Mechanical Engineering, Purdue University, West Lafayette, Indiana 47907, United States;* orcid.org/0000-0002-6125-2194

Sun Geun Yoon − *George W. Woodruff School of Mechanical Engineering, Georgia Institute of Technology, Atlanta, Georgia 30332, United States;* orcid.org/0000-0002-6222-8962

Bairav S. Vishnugopi − *School of Mechanical Engineering, Purdue University, West Lafayette, Indiana 47907, United States;* orcid.org/0009-0002-6357-9358

Congcheng Wang − *George W. Woodruff School of Mechanical Engineering, Georgia Institute of Technology, Atlanta, Georgia 30332, United States*

Talia A. Thomas − *George W. Woodruff School of Mechanical Engineering, Georgia Institute of Technology, Atlanta, Georgia 30332, United States*

Douglas Lars Nelson − *School of Materials Science and Engineering, Georgia Institute of Technology, Atlanta, Georgia 30332, United States;* orcid.org/0000-0003-3429-0547

Udochukwu D. Eze − *School of Materials Science and Engineering, Georgia Institute of Technology, Atlanta, Georgia 30332, United States;* orcid.org/0000-0002-4968-7689

Won Joon Jeong − *School of Materials Science and Engineering, Georgia Institute of Technology, Atlanta, Georgia 30332, United States*

John Harris − *School of Materials Science and Engineering, Georgia Institute of Technology, Atlanta, Georgia 30332, United States*

Partha P. Mukherjee − *School of Mechanical Engineering, Purdue University, West Lafayette, Indiana 47907, United States*

Complete contact information is available at: https://pubs.acs.org/10.1021/acsami.5c20956

Author Contributions

Conceptualization: E.P.A. and M.T.M.; Investigation: E.P.A., A.K.S., S.G.Y., B.S.V., C.W., T.A.T., D.L.N., U.C.E., W.J.J., and J.M.H.; Methodology: E.P.A., A.K.S., B.S.V., and M.T.M.; Formal Analysis: E.P.A., A.K.S., and B.S.V.; Validation: E.P.A., M.T.M., A.K.S., and B.S.V.; Visualization: E.P.A., M.T.M., A.K.S., and B.S.V.; Writing—original draft: E.P.A; Writing—review and editing: E.P.A, M.T.M., A.K.S., B.S.V., and P.P.M.; Supervision: M.T.M. and P.P.M.; Funding acquisition: M.T.M. and P.P.M.; Project administration: M.T.M. and P.P.M.

Notes

The authors declare no competing financial interest.

ACKNOWLEDGMENTS

This work was supported by the Center for Mechanochemical Understanding of Solid Ion Conductors (MUSIC), an Energy Frontier Research Center funded by the U.S. Department of Energy, Office of Science, Office of Basic Energy Sciences under contract DE-SC0023438. This document was prepared partly as a result of the use of facilities of the U.S. Department of Energy (DOE), which are managed by Brookhaven Science Associates, LLC, acting under Contract No. DE-SC0012704. Neither Brookhaven Science Associates, LLC, DOE, the U.S. Government, nor any person acting on their behalf (a) make any warranty or representation, express to the information contained in this document; or (b) assume any liabilities with respect to the use of, or damages resulting from, the use of any information contained in the document. This work was performed in part at the Georgia Tech Institute for Matter and Systems, a member of the National Nanotechnology Coordinated Infrastructure (NNCI), which is supported by the National Science Foundation (ECCS-2025462).

REFERENCES

(1) Bates, A. M.; Preger, Y.; Torres-Castro, L.; Harrison, K. L.; Harris, S. J.; Hewson, J. Are Solid-State Batteries Safer than Lithium-Ion Batteries? *Joule* **2022**, *6* (4), 742−755.

(2) Janek, J.; Zeier, W. G. Challenges in Speeding up Solid-State Battery Development. *Nat. Energy* **2023**, *8* (3), 230−240.

(3) Alsaç, E. P.; Nelson, D. L.; Yoon, S. G.; Cavallaro, K. A.; Wang, C.; Sandoval, S. E.; Eze, U. D.; Jeong, W. J.; McDowell, M. T. Characterizing Electrode Materials and Interfaces in Solid-State Batteries. *Chem. Rev.* **2025**, *125* (4), 2009−2119.

(4) Jangid, M. K.; Cho, T. H.; Ma, T.; Liao, D. W.; Kim, H.; Kim, Y.; Chi, M.; Dasgupta, N. P. Eliminating Chemo-Mechanical Degradation of Lithium Solid-State Battery Cathodes during > 4.5 V Cycling Using Amorphous Nb_2O_5 Coatings. *Nat. Commun.* **2024**, *15* (1), No. 10233.

(5) Liu, T.; Liu, J.; Li, L.; Yu, L.; Diao, J.; Zhou, T.; Li, S.; Dai, A.; Zhao, W.; Xu, S.; Ren, Y.; Wang, L.; Wu, T.; Qi, R.; Xiao, Y.; Zheng, J.; Cha, W.; Harder, R.; Robinson, I.; Wen, J.; Lu, J.; Pan, F.; Amine,

K. Origin of Structural Degradation in Li-Rich Layered Oxide Cathode. *Nature* **2022**, *606* (7913), 305−312.
(6) Zhou, H.; Xin, F.; Pei, B.; Whittingham, M. S. What Limits the Capacity of Layered Oxide Cathodes in Lithium Batteries? *ACS Energy Lett.* **2019**, *4* (8), 1902−1906.
(7) Liu, X.; Cheng, Y.; Su, Y.; Ren, F.; Zhao, J.; Liang, Z.; Zheng, B.; Shi, J.; Zhou, K.; Xiang, Y.; Zheng, J.; Wang, M.-S.; Huang, J.; Shao, M.; Yang, Y. Revealing the Surface-to-Bulk Degradation Mechanism of Nickel-Rich Cathode in Sulfide All-Solid-State Batteries. *Energy Storage Mater.* **2023**, *54*, 713−723.
(8) Han, G.-M.; Kim, Y.-S.; Ryu, H.-H.; Sun, Y.-K.; Yoon, C. S. Structural Stability of Single-Crystalline Ni-Rich Layered Cathode upon Delithiation. *ACS Energy Lett.* **2022**, *7* (9), 2919−2926.
(9) Zhou, J.; Holekevi Chandrappa, M. L.; Tan, S.; Wang, S.; Wu, C.; Nguyen, H.; Wang, C.; Liu, H.; Yu, S.; Miller, Q. R. S.; Hyun, G.; Holoubek, J.; Hong, J.; Xiao, Y.; Soulen, C.; Fan, Z.; Fullerton, E. E.; Brooks, C. J.; Wang, C.; Clément, R. J.; Yao, Y.; Hu, E.; Ong, S. P.; Liu, P. Healable and Conductive Sulfur Iodide for Solid-State Li−S Batteries. *Nature* **2024**, *627* (8003), 301−305.
(10) Song, H.; Münch, K.; Liu, X.; Shen, K.; Zhang, R.; Weintraut, T.; Yusim, Y.; Jiang, D.; Hong, X.; Meng, J.; Liu, Y.; He, M.; Li, Y.; Henkel, P.; Brezesinski, T.; Janek, J.; Pang, Q. All-Solid-State Li−S Batteries with Fast Solid−Solid Sulfur Reaction. *Nature* **2025**, *637* (8047), 846−853.
(11) Whang, G.; Zeier, W. G. Transition Metal Sulfide Conversion: A Promising Approach to Solid-State Batteries. *ACS Energy Lett.* **2023**, *8* (12), 5264−5274.
(12) Dewald, G. F.; Liaqat, Z.; Lange, M. A.; Tremel, W.; Zeier, W. G. Influence of Iron Sulfide Nanoparticle Sizes in Solid-State Batteries. *Angew. Chem.* **2021**, *133* (33), 18096−18100.
(13) Wu, Z.; Zhang, W.; Xia, Y.; Huang, H.; Gan, Y.; He, X.; Xia, X.; Zhang, J. A Comprehensive Cognition for the Capacity Fading Mechanism of FeS_2 in Argyrodite-Based All-Solid-State Lithium Battery. *EcoMat* **2023**, *5* (4), No. e12327.
(14) Zhang, Z.; Dong, K.; Mazzio, K. A.; Hilger, A.; Markötter, H.; Wilde, F.; Heinemann, T.; Manke, I.; Adelhelm, P. Phase Transformation and Microstructural Evolution of CuS Electrodes in Solid-State Batteries Probed by In Situ 3D X-Ray Tomography. *Adv. Energy Mater.* **2023**, *13* (2), No. 2203143.
(15) Shao, B.; Tan, S.; Huang, Y.; Zhang, L.; Shi, J.; Yang, X.-Q.; Hu, E.; Han, F. Enabling Conversion-Type Iron Fluoride Cathode by Halide-Based Solid Electrolyte. *Adv. Funct. Mater.* **2022**, *32* (49), No. 2206845.
(16) Hu, J.; Lei, M.; Zhu, C.; Zhang, B.; Li, C. Highly Conductive Doped Fluoride Solid Electrolytes with Solidified Ionic Liquid to Enable Reversible FeF_3 Conversion Solid State Batteries. *Adv. Funct. Mater.* **2024**, *34* (41), No. 2314044.
(17) Peng, J.; Wang, X.; Li, H.; Chen, L.; Wu, F. High-Capacity, Long-Life Iron Fluoride All-Solid-State Lithium Battery with Sulfide Solid Electrolyte. *Adv. Energy Mater.* **2023**, *13* (23), No. 2300706.
(18) Inoishi, A.; Setoguchi, N.; Hori, H.; Kobayashi, E.; Sakamoto, R.; Sakaebe, H.; Okada, S. FeF_3 as Reversible Cathode for All-Solid-State Fluoride Batteries. *Adv. Energy Sustainability Res.* **2022**, *3* (12), No. 2200131.
(19) Kim, J. T.; Su, H.; Zhong, Y.; Wang, C.; Wu, H.; Zhao, D.; Wang, C.; Sun, X.; Li, Y. All-Solid-State Lithium−Sulfur Batteries through a Reaction Engineering Lens. *Nat. Chem. Eng.* **2024**, *1* (6), 400−410.
(20) Pan, H.; Cheng, Z.; He, P.; Zhou, H. A Review of Solid-State Lithium−Sulfur Battery: Ion Transport and Polysulfide Chemistry. *Energy Fuels* **2020**, *34* (10), 11942−11961.
(21) Huang, Y.; Lin, L.; Zhang, C.; Liu, L.; Li, Y.; Qiao, Z.; Lin, J.; Wei, Q.; Wang, L.; Xie, Q.; Peng, D.-L. Recent Advances and Strategies toward Polysulfides Shuttle Inhibition for High-Performance Li−S Batteries. *Adv. Sci.* **2022**, *9* (12), No. 2106004.
(22) Li, S.; Zhang, W.; Zheng, J.; Lv, M.; Song, H.; Du, L. Inhibition of Polysulfide Shuttles in Li−S Batteries: Modified Separators and Solid-State Electrolytes. *Adv. Energy Mater.* **2021**, *11* (2), No. 2000779.
(23) Li, Z.; Zhou, G.; Li, S.; Liu, H.; Wang, L.; Li, H. Unlocking Cycling Longevity in Micro-Sized Conversion-Type FeS_2 Cathodes. *Joule* **2023**, *7* (11), 2609−2621.
(24) Wei, C.; Wang, R.; Wu, Z.; Luo, Q.; Jiang, Z.; Ming, L.; Yang, J.; Wang, L.; Yu, C. Revealing the Size Effect of FeS_2 on Solid-State Battery Performances at Different Operating Temperatures. *Chin. Chem. Lett.* **2024**, *35* (6), No. 108717.
(25) Wang, D.; Gwalani, B.; Wierzbicki, D.; Singh, V.; Jhang, L.-J.; Rojas, T.; Kou, R.; Liao, M.; Ye, L.; Jiang, H.; Shan, S.; Silver, A.; Ngo, A. T.; Du, Y.; Li, X.; Wang, D. Overcoming the Conversion Reaction Limitation at Three-Phase Interfaces Using Mixed Conductors towards Energy-Dense Solid-State Li−S Batteries. *Nat. Mater.* **2025**, *24*, 243−251.
(26) Yu, Z.; Singh, B.; Yu, Y.; Nazar, L. F. Suppressing Argyrodite Oxidation by Tuning the Host Structure for High-Areal-Capacity All-Solid-State Lithium−Sulfur Batteries. *Nat. Mater.* **2025**, *24*, 1082−1090.
(27) Cao, Y.; Geng, C.; Bai, C.; Peng, L.; Lan, J.; Liu, J.; Han, J.; Liu, B.; He, Y.; Kang, F.; Yang, Q.-H.; Lv, W. Integrating Solid Interfaces for Catalysis in All-Solid-State Lithium−Sulfur Batteries. *Energy Environ. Sci.* **2025**, *18* (8), 3795−3806.
(28) Ohno, S.; Zeier, W. G. Toward Practical Solid-State Lithium−Sulfur Batteries: Challenges and Perspectives. *Acc. Mater. Res.* **2021**, *2* (10), 869−880.
(29) Boebinger, M. G.; Yeh, D.; Xu, M.; Miles, B. C.; Wang, B.; Papakyriakou, M.; Lewis, J. A.; Kondekar, N. P.; Cortes, F. J. Q.; Hwang, S.; Sang, X.; Su, D.; Unocic, R. R.; Xia, S.; Zhu, T.; McDowell, M. T. Avoiding Fracture in a Conversion Battery Material through Reaction with Larger Ions. *Joule* **2018**, *2* (9), 1783−1799.
(30) Fujita, Y.; Münch, K.; Asakura, T.; Motohashi, K.; Sakuda, A.; Janek, J.; Hayashi, A. Dynamic Volume Change of Li_2S-Based Active Material and the Influence of Stacking Pressure on Capacity in All-Solid-State Batteries. *Chem. Mater.* **2024**, *36* (15), 7533−7540.
(31) Xiao, R.; Qu, Z.; Ren, J.; Wang, G.; Sun, Z.; Li, F. Current Status and Future Prospects of Solid-State Lithium−Sulfur Batteries: A Focus on Reaction and Interface Engineering. *Adv. Energy Mater.* **2025**, No. 2501926.
(32) Sun, N.; Liu, Q.; Cao, Y.; Lou, S.; Ge, M.; Xiao, X.; Lee, W.-K.; Gao, Y.; Yin, G.; Wang, J.; Sun, X. Anisotropically Electrochemical−Mechanical Evolution in Solid-State Batteries and Interfacial Tailored Strategy. *Angew. Chem., Int. Ed.* **2019**, *58* (51), 18647−18653.
(33) Pavan, M.; Münch, K.; Benz, S. L.; Bernges, T.; Henss, A.; Zeier, W. G.; Janek, J. Role and Evolution of FeS_2 Cathode Microstructure in Argyrodite-Based All-Solid-State Lithium−Sulfur Batteries. *Chem. Mater.* **2025**, *37* (9), 3185−3196.
(34) Ohno, S.; Koerver, R.; Dewald, G.; Rosenbach, C.; Titscher, P.; Steckermeier, D.; Kwade, A.; Janek, J.; Zeier, W. G. Observation of Chemomechanical Failure and the Influence of Cutoff Potentials in All-Solid-State Li−S Batteries. *Chem. Mater.* **2019**, *31* (8), 2930−2940.
(35) Qu, H.; Ding, T.; Zhang, X.; Qiu, D.; Chen, P.; Zheng, D.; Lu, D.; Qu, D. Deciphering Volume Changes in Li-S Solid-State Battery Components during Cycling: Implication for Advanced Battery Design. *Nano Energy* **2025**, *138*, No. 110887.
(36) Gu, J.; Hu, W.; Wu, Y.; Ren, F.; Liang, Z.; Zhong, H.; Zheng, X.; Ma, R.; Luo, Y.; Chen, X.; Shi, J.; Yang, Y. Asymmetric Sulfur Redox Paths in Sulfide-Based All-Solid-State Lithium−Sulfur Batteries. *Chem. Mater.* **2024**, *36* (9), 4403−4416.
(37) Barai, P.; Mistry, A.; Mukherjee, P. P. Poromechanical Effect in the Lithium−Sulfur Battery Cathode. *Extreme Mech. Lett.* **2016**, *9*, 359−370.
(38) Han, S. Y.; Lee, C.; Lewis, J. A.; Yeh, D.; Liu, Y.; Lee, H.-W.; McDowell, M. T. Stress Evolution during Cycling of Alloy-Anode Solid-State Batteries. *Joule* **2021**, *5* (9), 2450−2465.
(39) Lee, C.; Han, S. Y.; Lewis, J. A.; Shetty, P. P.; Yeh, D.; Liu, Y.; Klein, E.; Lee, H.-W.; McDowell, M. T. Stack Pressure Measurements to Probe the Evolution of the Lithium−Solid-State Electrolyte Interface. *ACS Energy Lett.* **2021**, *6* (9), 3261−3269.

https://doi.org/10.1021/acsami.5c20956
ACS Appl. Mater. Interfaces 2026, 18, 1626−1640

(40) Jung, S.-J.; Lee, C.; Park, C.; Ryu, S.; Lee, J.; Kang, M.-G.; Kim, E.; Kim, J. Y.; Bae, K. Y.; Son, S.; Lee, H.-W. Lithiation Diagnostics by Measuring Electrochemodynamics in Solid-State Batteries. *ACS Energy Lett.* **2025**, *10*, 3112−3121.
(41) Lee, C.; Kim, J. Y.; Bae, K. Y.; Kim, T.; Jung, S.-J.; Son, S.; Lee, H.-W. Enhancing Electrochemomechanics: How Stack Pressure Regulation Affects All-Solid-State Batteries. *Energy Storage Mater.* **2024**, *66*, No. 103196.
(42) Jun, S.; Nam, Y. J.; Kwak, H.; Kim, K. T.; Oh, D. Y.; Jung, Y. S. Operando Differential Electrochemical Pressiometry for Probing Electrochemo-Mechanics in All-Solid-State Batteries. *Adv. Funct. Mater.* **2020**, *30* (31), No. 2002535.
(43) Lim, H.; Jun, S.; Song, Y. B.; Baeck, K. H.; Bae, H.; Lee, G.; Kim, J.; Jung, Y. S. Rationally Designed Conversion-Type Lithium Metal Protective Layer for All-Solid-State Lithium Metal Batteries. *Adv. Energy Mater.* **2024**, *14* (12), No. 2303762.
(44) Wu, D.; Alsaç, E. P.; Claus, A.; Fang, Z.; Jangid, M. K.; Lee, K.; Nelson, D. L.; Park, S. H.; Zhang, S.; Chi, M.; Dasgupta, N. P.; McDowell, M. T.; Perry, N. H.; Sakamoto, J.; Hatzell, K. B. The State of Reliable Characterization and Testing of Solid-State Batteries. *ACS Energy Lett.* **2025**, *10*, 2617−2630.
(45) Yoon, S. G.; Vishnugopi, B. S.; Nelson, D. L.; Yong, A. X. B.; Wang, Y.; Sandoval, S. E.; Thomas, T. A.; Cavallaro, K. A.; Shevchenko, P.; Alsaç, E. P.; Wang, C.; Singla, A.; Greer, J. R.; Ertekin, E.; Mukherjee, P. P.; McDowell, M. T. Interface Morphogenesis with a Deformable Secondary Phase in Solid-State Lithium Batteries. *Science* **2025**, *388* (6751), 1062−1068.
(46) Yoon, S. G.; Vishnugopi, B. S.; Alsaç, E. P.; Jeong, W. J.; Sandoval, S. E.; Nelson, D. L.; Ayyaswamy, A.; Mukherjee, P. P.; McDowell, M. T. Synergistic Evolution of Alloy Nanoparticles and Carbon in Solid-State Lithium Metal Anode Composites at Low Stack Pressure. *ACS Nano* **2024**, *18* (31), 20792−20805.
(47) Wang, C.; Liu, Y.; Jeong, W. J.; Chen, T.; Lu, M.; Nelson, D. L.; Alsaç, E. P.; Yoon, S. G.; Cavallaro, K. A.; Das, S.; Majumdar, D.; Gopalaswamy, R.; Xia, S.; McDowell, M. T. The Influence of Pressure on Lithium Dealloying in Solid-State and Liquid Electrolyte Batteries. *Nat. Mater.* **2025**, *24*, 907−916.
(48) Xu, G.; Yan, Z.; Yang, H.; Zhang, X.; Su, Y.; Huang, Z.; Zhang, L.; Tang, Y.; Wang, Z.; Zhu, L.; Lin, J.; Yang, L.; Huang, J. Multiscale Structural Engineering of Sulfur/Carbon Cathodes Enables High Performance All-Solid-State Li-S Batteries. *Small* **2023**, *19* (30), No. 2300420.
(49) Bai, X.; Jiang, D.; Yin, S.; Hao, Y.; Zheng, J.; Hao, H.; Xing, J.; Dong, J.; Liu, H.; Liao, L. Pyrite-Based Solid-State Batteries: Progresses, Challenges, and Perspectives. *Adv. Funct. Mater.* **2025**, *35* (10), No. 2416808.
(50) Lee, J.; Zhou, S.; Ferrari, V. C.; Zhao, C.; Sun, A.; Nicholas, S.; Liu, Y.; Sun, C.; Wierzbicki, D.; Parkinson, D. Y.; Bai, J.; Xu, W.; Du, Y.; Amine, K.; Xu, G.-L. Halide Segregation to Boost All-Solid-State Lithium-Chalcogen Batteries. *Science* **2025**, *388* (6748), 724−729.
(51) Haslam, C. G.; Wolfenstine, J. B.; Sakamoto, J. The Effect of Aspect Ratio on the Mechanical Behavior of Li Metal in Solid-State Cells. *J. Power Sources* **2022**, *520*, No. 230831.
(52) Koerver, R.; Zhang, W.; Biasi, L. de.; Schweidler, S.; O Kondrakov, A.; Kolling, S.; Brezesinski, T.; Hartmann, P.; G Zeier, W.; Janek, J. Chemo-Mechanical Expansion of Lithium Electrode Materials − on the Route to Mechanically Optimized All-Solid-State Batteries. *Energy Environ. Sci.* **2018**, *11* (8), 2142−2158.
(53) Ravel, B.; Newville, M. Athena, Artemis, Hephaestus: Data Analysis for X-Ray Absorption Spectroscopy Using IFEFFIT. *J. Synchrotron Radiat* **2005**, *12* (Pt 4), 537−541.
(54) Mistry, A.; Mukherjee, P. P. Precipitation−Microstructure Interactions in the Li-Sulfur Battery Electrode. *J. Phys. Chem. C* **2017**, *121* (47), 26256−26264.
(55) Liu, Z.; Mukherjee, P. P. Mesoscale Elucidation of Surface Passivation in the Li−Sulfur Battery Cathode. *ACS Appl. Mater. Interfaces* **2017**, *9* (6), 5263−5271.
(56) Liu, Z.; Balbuena, P. B.; Mukherjee, P. P. Revealing Charge Transport Mechanisms in Li_2S_2 for Li−Sulfur Batteries. *J. Phys. Chem. Lett.* **2017**, *8* (7), 1324−1330.
(57) Kim, J. T.; Rao, A.; Nie, H.-Y.; Hu, Y.; Li, W.; Zhao, F.; Deng, S.; Hao, X.; Fu, J.; Luo, J.; Duan, H.; Wang, C.; Singh, C. V.; Sun, X. Manipulating Li_2S_2/Li_2S Mixed Discharge Products of All-Solid-State Lithium Sulfur Batteries for Improved Cycle Life. *Nat. Commun.* **2023**, *14* (1), No. 6404.
(58) Kim, H.; Choi, H.-N.; Hwang, J.-Y.; Yoon, C. S.; Sun, Y.-K. Tailoring the Interface between Sulfur and Sulfide Solid Electrolyte for High-Areal-Capacity All-Solid-State Lithium−Sulfur Batteries. *ACS Energy Lett.* **2023**, *8* (10), 3971−3979.
(59) Puls, S.; Nazmutdinova, E.; Kalyk, F.; Woolley, H. M.; Thomsen, J. F.; Cheng, Z.; Fauchier-Magnan, A.; Gautam, A.; Gockeln, M.; Ham, S.-Y.; Hasan, M. T.; Jeong, M.-G.; Hiraoka, D.; Kim, J. S.; Kutsch, T.; Lelotte, B.; Minnmann, P.; Miß, V.; Motohashi, K.; Nelson, D. L.; Ooms, F.; Piccolo, F.; Plank, C.; Rosner, M.; Sandoval, S. E.; Schlautmann, E.; Schuster, R.; Spencer-Jolly, D.; Sun, Y.; Vishnugopi, B. S.; Zhang, R.; Zheng, H.; Adelhelm, P.; Brezesinski, T.; Bruce, P. G.; Danzer, M.; El Kazzi, M.; Gasteiger, H.; Hatzell, K. B.; Hayashi, A.; Hippauf, F.; Janek, J.; Jung, Y. S.; McDowell, M. T.; Meng, Y. S.; Mukherjee, P. P.; Ohno, S.; Roling, B.; Sakuda, A.; Schwenzel, J.; Sun, X.; Villevieille, C.; Wagemaker, M.; Zeier, W. G.; Vargas-Barbosa, N. M. Benchmarking the Reproducibility of All-Solid-State Battery Cell Performance. *Nat. Energy* **2024**, *9* (10), 1310−1320.
(60) Wang, X.; Wang, Z.; Chen, L.; Li, H.; Wu, F. High-Capacity Sulfide All-Solid-State Lithium Battery with a Conversion-Type Iron Fluoride Cathode. *J. Mater. Chem. A* **2023**, *11* (8), 4142−4154.
(61) Krauskopf, T.; Richter, F. H.; Zeier, W. G.; Janek, J. Physicochemical Concepts of the Lithium Metal Anode in Solid-State Batteries. *Chem. Rev.* **2020**, *120* (15), 7745−7794.
(62) Strauss, F.; de Biasi, L.; Kim, A.-Y.; Hertle, J.; Schweidler, S.; Janek, J.; Hartmann, P.; Brezesinski, T. Rational Design of Quasi-Zero-Strain NCM Cathode Materials for Minimizing Volume Change Effects in All-Solid-State Batteries. *ACS Mater. Lett.* **2020**, *2* (1), 84−88.
(63) Wang, D.; Jhang, L.-J.; Kou, R.; Liao, M.; Zheng, S.; Jiang, H.; Shi, P.; Li, G.-X.; Meng, K.; Wang, D. Realizing High-Capacity All-Solid-State Lithium-Sulfur Batteries Using a Low-Density Inorganic Solid-State Electrolyte. *Nat. Commun.* **2023**, *14* (1), No. 1895.
(64) Alt, C. D.; Keuntje, S.; Schneider, I. L.; Westphal, J.; Minnmann, P.; Eckhardt, J. K.; Peppler, K.; Janek, J. In−Li Counter Electrodes in Solid-State Batteries − A Comparative Approach on Kinetics, Microstructure, and Chemomechanics. *Adv. Energy Mater.* **2025**, *15* (12), No. 2404055.
(65) Zou, J.; Zhao, J.; Wang, B.; Chen, S.; Chen, P.; Ran, Q.; Li, L.; Wang, X.; Yao, J.; Li, H.; Huang, J.; Niu, X.; Wang, L. Unraveling the Reaction Mechanism of FeS_2 as a Li-Ion Battery Cathode. *ACS Appl. Mater. Interfaces* **2020**, *12* (40), 44850−44857.
(66) Mwizerwa, J. P.; Zhang, Q.; Han, F.; Wan, H.; Cai, L.; Wang, C.; Yao, X. Sulfur-Embedded FeS_2 as a High-Performance Cathode for Room Temperature All-Solid-State Lithium−Sulfur Batteries. *ACS Appl. Mater. Interfaces* **2020**, *12* (16), 18519−18525.
(67) Bradbury, R.; Dewald, G. F.; Kraft, M. A.; Arlt, T.; Kardjilov, N.; Janek, J.; Manke, I.; Zeier, W. G.; Ohno, S. Visualizing Reaction Fronts and Transport Limitations in Solid-State Li−S Batteries via Operando Neutron Imaging. *Adv. Energy Mater.* **2023**, *13* (17), No. 2203426.
(68) Sharma, A. K.; Vishnugopi, B. S.; Ayyaswamy, A.; Nath, A.; Chatterjee, D.; Tewari, D.; Ng, M. S.; Tang, W. S.; Premnath, V.; Jeevarajan, J. A.; Mukherjee, P. P. Co-Design of Active Material and Solid Electrolyte Particulate Phases in Solid-State Battery Composite Electrodes. *ACS Appl. Mater. Interfaces* **2025**, *17* (35), 49520−49532.
(69) Hua, X.; Eggeman, A. S.; Castillo-Martínez, E.; Robert, R.; Geddes, H. S.; Lu, Z.; Pickard, C. J.; Meng, W.; Wiaderek, K. M.; Pereira, N.; Amatucci, G. G.; Midgley, P. A.; Chapman, K. W.; Steiner, U.; Goodwin, A. L.; Grey, C. P. Revisiting Metal Fluorides as Lithium-Ion Battery Cathodes. *Nat. Mater.* **2021**, *20* (6), 841−850.

(70) Jonane, I.; Timoshenko, J.; Kuzmin, A. Atomistic Simulations of the Fe K-Edge EXAFS in FeF_3 Using Reverse Monte Carlo Methods. *Phys. Scr.* **2016**, *91* (10), No. 104001.
(71) Kostov, S.; denBoer, M.; Strauss, E.; Golodnitsky, D.; Greenbaum, S. G.; Peled, E. X-Ray Absorption Fine Structure Studies of FeS_2 Cathodes in Lithium Polymer Electrolyte Batteries. *J. Power Sources* **1999**, *81*−*82*, 709−714.
(72) Butala, M. M.; Mayo, M.; Doan-Nguyen, V. V. T.; Lumley, M. A.; Göbel, C.; Wiaderek, K. M.; Borkiewicz, O. J.; Chapman, K. W.; Chupas, P. J.; Balasubramanian, M.; Laurita, G.; Britto, S.; Morris, A. J.; Grey, C. P.; Seshadri, R. Local Structure Evolution and Modes of Charge Storage in Secondary Li−FeS_2 Cells. *Chem. Mater.* **2017**, *29* (7), 3070−3082.
(73) Womes, M.; Karnatak, R. C.; Esteva, J. M.; Lefebvre, I.; Allan, G.; Olivier-fourcades, J.; Jumas, J. C. Electronic Structures of FeS and FeS_2: X-Ray Absorption Spectroscopy and Band Structure Calculations. *J. Phys. Chem. Solids* **1997**, *58* (2), 345−352.
(74) Xie, L.; Zhang, X.; Hu, H.; Chen, J.; Zhang, Y.; Xiao, P.; He, X.; Wang, Z.; Gu, H.; Huang, J.; Huang, Q. Improved Interfacial Stability of an Iron Trifluoride Cathode with a Yolk−Shell Structure in Sulfide-Based All-Solid-State Lithium Batteries. *ACS Appl. Mater. Interfaces* **2025**, *17* (22), 33036−33046.
(75) Ali, G.; Lee, J.-H.; Chang, W.; Cho, B.-W.; Jung, H.-G.; Nam, K.-W.; Chung, K. Y. Lithium Intercalation Mechanism into $FeF_3 \cdot 0.5H_2O$ as a Highly Stable Composite Cathode Material. *Sci. Rep.* **2017**, *7* (1), No. 42237.

https://doi.org/10.1021/acsami.5c20956
ACS Appl. Mater. Interfaces 2026, 18, 1626−1640